Epitaxial growth and magnetic properties of Fe4−xMnxN thin films grown on MgO(0?0?1) substrates by molecular beam epitaxy

doi: 10.1016/j.jcrysgro.2018.02.037

Epitaxial growth and magnetic properties of $Fe_{4-x}Mn_xN$ thin films grown on MgO(001) substrates by molecular beam epitaxy

Akihito Anzai[a], Fumiya Takata[a], Toshiki Gushi[a], Kaoru Toko[a], and Takashi Suemasu[a]

[a]*Institute of Applied Physics, Graduate School of Pure and Applied Sciences, University of Tsukuba, Tsukuba, Ibaraki 305-8573, Japan*

Epitaxial $Fe_{4-x}Mn_xN$ (x = 0, 1, 2, 3, and 4) thin films were successfully grown on MgO(001) single-crystal substrates by molecular beam epitaxy, and their crystalline qualities and magnetic properties were investigated. It was found that the lattice constants of $Fe_{4-x}Mn_xN$ obtained from X-ray diffraction measurement increased with the Mn content. The ratio of the perpendicular lattice constant c to the in-plane lattice constant a of $Fe_{4-x}Mn_xN$ was found to be about 0.99 at $x \geq 2$. The magnetic properties evaluated using a vibrating sample magnetometer at room temperature revealed that all of the $Fe_{4-x}Mn_xN$ films exhibited ferromagnetic behavior regardless of the value of x. In addition, the saturation magnetization decreased non-linearly as the Mn content increased. Finally, $FeMn_3N$ and Mn_4N exhibited perpendicular anisotropy and their uniaxial magnetic anisotropy energies were 2.2×10^5 and 7.5×10^5 erg/cm^3, respectively.

* Corresponding author.

Electronic mail: suemasu@bk.tsukuba.ac.jp

Keywords: A3.Molecular beam epitaxy; B1.Fe_4N; B1.MgO; B1.Mn_4N;

1. Introduction

Spin-transfer torque magnetic random access memory (STT-MRAM) has attracted attention for new spintronics devices such as nonvolatile memory. Ferromagnetic thin films with large perpendicular magnetic anisotropy (PMA) and low saturation magnetization (M_S) are required for magnetization switching with small currents in STT-MRAM [1,2]. Anti-perovskite nitrides and their mixed crystals have been focused as spintronics material both with theory and experiments [3-12]. One of these anti-perovskite ferrimagnetic nitrides, Mn_4N, satisfies both requirements of a PMA and a small M_S. A PMA has been reported for Mn_4N films grown on glass [13], Si(001) [14], MgO(001) [15-19], and $SrTiO_3$(STO)(001) [15,20] substrates. Further, the Mn_4N bulk is a ferrimagnetic metal (M_S = 182 emu/cm^3 at 77 K) with a high Curie temperature of 745 K [3]. The lattice structure of Mn_4N is shown in Fig. 1, wherein the Mn atoms occupy the corner (I) and face-centered (II) sites and the N atom occupies the body-centered site. The II sites of Mn_4N are further divided into IIA and IIB sites in the presence of magnetization (arrow in Fig. 1). The magnetic moments of the Mn atoms have been evaluated as 3.85 μ_B at the I sites and –0.90 μ_B at the II sites from neutron diffraction measurements obtained at 77 K [3], where μ_B is the Bohr magneton. In contrast to that found in the Mn_4N bulk, in Mn_4N films the ratio of the perpendicular lattice constant c to the in-plane lattice constant a, c/a = 0.99 regardless of the film thickness [15]. Substitution of other 3d transition metal atoms for the Mn in Mn_4N is an effective means to modify the magnetic properties. For instance, superior magnetic and mechanical properties were predicted by first-principles calculations for Fe_3MnN [21-23], which is isostructural with Mn_4N. Further, the Mössbauer measurement revealed that Mn is likely to occupy the I site of $Fe_{4-x}Mn_xN$ (where x = 0–0.75) [24]. In particular, Fe_4N is a ferromagnetic nitride with a very large negative spin polarization of the electrical conductivity (P_σ = –1.0) [6], where this high spin polarization was confirmed via point-contact Andreev reflection ($|P_\sigma|$ = 0.59) [25] and with the inverse tunnel

magnetoresistance effect of 75% in Fe_4N/MgO/CoFeB magnetic tunnel junctions [26]. Although the magnetic properties of $Fe_{4-x}Mn_xN$ have been theoretically anticipated [21-23], its formation has been limited to powders with a small Mn content ($x \leq 0.75$), and no reports have been made on the epitaxial growth of $Fe_{4-x}Mn_xN$ with larger x. In this work, we aim to grow $Fe_{4-x}Mn_xN$ (where x = 0, 1, 2, 3 and 4) epitaxial films by molecular beam epitaxy (MBE) and characterize their magnetic properties.

2. Experimental

30 nm-thick $Fe_{4-x}Mn_xN$ (x = 0, 1, 2, 3, and 4) thin films were grown on MgO(001) single-crystal substrates by MBE using solid sources of Mn and Fe and radio-frequency N plasma. The substrate temperature (T_{sub}) was varied from 350–550 °C to determine the optimum temperature for each composition. Figure 2 shows a representative emission spectrum of nitrogen plasma obtained at 108 W, as measured by a spectrometer (QE Pro; Ocean Optics, Inc.). Many nitrogen species exist in the plasma, such as the first-excited neutral N_2, higher-excited neutral N_2, N_2^+ ions and atomic N. Three regions are observed to exist in the spectrum, and are labeled as regions denoting ions, molecules and atoms in Fig. 2. According to Ref. [27], the emissions in the wavelength λ ranging from 700–800 nm correspond to the atomic N, and this is therefore labeled as the atoms region in Fig. 2. Among these three regions, we used the emission intensity at λ = 336 nm, denoted as I_N, as a measure and set it to be a constant for all spectra. Nitrogen ions were eliminated by applying bias voltages to the plasma generator, while the Mn/Fe ratio was controlled by the deposition rate (nm/min) based on the crucible temperature of the Knudsen cells. The crystalline quality of the samples was evaluated by reflection high-energy electron diffraction (RHEED), out-of-plane (θ–2θ) X-ray diffraction (XRD; Smart-Lab, Rigaku Inc.), X-ray ω-scan rocking curve, and in-plane (φ–$2\theta\chi$) XRD measurement with Cu-$K\alpha$ radiation. In these X-ray measurements, a Ge(220) single crystal was used to monochromatize the X-ray. The root-mean-square (RMS) surface roughness of grown

films was measured by atomic force microscopy. The magnetization versus magnetic field curves (*M–H* curves) were measured by a vibrating sample magnetometer (VSM) at room temperature (RT). To calculate the sample thickness excluding the surface oxidation layer, we used an X-ray reflectivity measurement.

3. Results and discussion

Figure 3 shows the out-of-plane XRD and RHEED patterns of 30 nm-thick $Fe_{4-x}Mn_xN$ (x = 0, 1, 2, 3, and 4) films grown at T_{sub} = 450 °C for x = 0 and 2 and 550 °C for x = 1, 3, and 4. The reason these T_{sub} values were chosen is that the full width at half maximum (FWHM) of the $Fe_{4-x}Mn_xN$(002) diffraction peaks were minimized at these temperatures for each nitride phase. Those FWHM values reached 1.17°, 1.26°, 1.43°, 1.10°, and 1.85° for x = 0, 1, 2, 3, and 4 in $Fe_{4-x}Mn_xN$, respectively. The RMS surface roughness values were smaller than 1 nm; they were 0.418, 0.946, 0.945, 0.186, and 0.691 nm, respectively. Streaky RHEED patterns and *c*-axis-oriented XRD diffraction peaks corresponding to the nitrides phase were observed for all of the samples, indicating that single-phase nitrides were epitaxially grown on the MgO(001) substrates. In the RHEED patterns of Fig. 3, superlattice diffractions from N atom at body-center site marked by arrows were clearly observed in Mn_4N, Fe_3MnN, and Fe_4N films, which indicates the N atoms were long-range ordered, whereas those lines were blurred in the $FeMn_3N$ and Fe_2Mn_2N films. In the XRD patterns, however, the (001) superlattice peaks appeared in all the samples, representing the presence of N atom at the correct position in those films. The (001)-oriented diffraction peaks of $Fe_{4-x}Mn_xN$ shifted to lower angles with the Mn content, signifying that the lattice constant *c* increased. This shift results from Mn_4N possessing a larger lattice constant than Fe_4N.

Figure 4 shows the in-plane XRD patterns of the $Fe_{4-x}Mn_xN$ films. The incident x-ray angle was fixed at ω = 0.4° and the scattering vector was set along MgO [200], where the diffraction peak of β-Mn was observed in the Mn_4N film around $2\theta\chi$ = 75°. It is supposed that

the low flux ratio of N_2 to Mn caused the unreacted Mn to become crystallized [18]. In this work, however, we put more emphasis on getting the smallest FWHM value of $Fe_{4-x}Mn_xN$ XRD peak for each composition rather than achieving single-phase $Fe_{4-x}Mn_xN$. According to Dhar *et al*.[28], the epitaxial growth of single-phase Mn_4N films without metallic inclusions was achieved on 6H-SiC(0001) and GaN(0001) substrates by MBE using NH_3. We also observed a diffraction peak of α–Fe at $2\theta\chi = 45°$ in Fe_3MnN, which was similar to the segregation of α-Fe with increasing Mn content observed in the powdered $Fe_{4-x}Mn_xN$ (x = 0–0.75) [24]. The diffraction peak of (100)-oriented $Fe_{4-x}Mn_xN$ shifted to lower angles with Mn content, signifying that the in-plane lattice constants a and b increased. Figure 5 shows these lattice parameters and the ratio c/a as determined by Cohen's method adapting the Nelson-Riley function [29]. For the $Fe_{4-x}Mn_xN$ ($x \geq 2$), the c/a was found to be approximately 0.99, indicating the presence of in-plane tensile strain.

Figure 6 shows the M–H curves of $Fe_{4-x}Mn_xN$ as measured by VSM at RT for H applied in the direction perpendicular to the plane (Fig. 6(a)) and for H applied in the in-plane direction (Fig. 6(b)). All $Fe_{4-x}Mn_xN$ films exhibited ferromagnetic behavior and, further, Mn_4N and $FeMn_3N$ exhibited PMA. The hysteresis curve of Mn_4N was distinctly opened when H was applied normal to the film, demonstrating the occurrence of PMA. In $FeMn_3N$, the magnetization saturated at a smaller H when H was applied in the direction normal to the sample surface than that in the in-plane direction. However, $Fe_{4-x}Mn_xN$ ($x \leq 2$) exhibited in-plane magnetic anisotropy.

Figure 7 shows the value of the M_S of $Fe_{4-x}Mn_xN$ as a function of the value of x, which is seen to decrease nonlinearly with Mn content, exhibiting M_S values of 1170, 714, 391, 135 and 103 emu/cm^3 at x = 0, 1, 2, 3 and 4, respectively. This result is different from the theoretical prediction that $FeMn_3N$ is antiferromagnet [22]. The M_S of Mn_4N (103 emu/cm^3) was slightly smaller than the 110 emu/cm^3 value obtained for Mn_4N films grown by the reactive sputtering method [18], which was probably caused by the Mn precipitation depicted in Fig. 4. We

calculated the uniaxial magnetic anisotropy energy (K_u) for each area surrounding the magnetization easy axis, hard axis, and the vertical M axis in the first quadrant of Figs. 6(a) and 6(b). It was found that the K_u increased with Mn content, exhibiting values of 2.2×10^5 and 7.5×10^5 erg/cm^3 for $FeMn_3N$ and Mn_4N, respectively. This K_u value for Mn_4N was a little lower than that of 8.8×10^5 erg/cm^3 reported in Ref. [18]. We speculate that the lower K_u value in this work is also owing to unreacted Mn. Note that such metallic inclusions were not detected in the materials of prime interest in this work such as $FeMn_3N$ and Fe_2Mn_2N as shown in Figs. 3 and 4.

4. Conclusion

Epitaxial thin films of $Fe_{4-x}Mn_xN$ (x = 0, 1, 2, 3, and 4) were successfully prepared on an MgO(001) single-crystal substrate and their magnetic properties were investigated. The in-plane and out-of-plane lattice constants of the $Fe_{4-x}Mn_xN$ films increased with Mn content. Further, an in-plane tensile strain of c/a ~ 0.99 was present in $Fe_{4-x}Mn_xN$ films with x = 2, 3, and 4. The value of M_S decreased with Mn content non-linearly, while all $Fe_{4-x}Mn_xN$ films ($0 \leq x \leq 4$) exhibited ferromagnetic behavior and PMA occurred in $FeMn_3N$ and Mn_4N. Finally, the K_u value was 2.2×10^5 erg/cm^3 for $FeMn_3N$ and 7.5×10^5 erg/cm^3 for Mn_4N.

Acknowledgments

This work was financially supported in part by the Japan Society for the Promotion of Science (JSPS) Grants-in-Aid for Scientific Research (A) (No. 26249037) and by JSPS Fellows (No. 16J02879). The VSM measurements were performed with the help of Professor H. Yanagihara of the University of Tsukuba.

References

[1] A. Mangin, D. Ravelosona, J. A. Katine, M. J. Carey, B. D. Terris, Eric E. Fullerton, Nat. Mater. 5 (2006) 210.

[2] S. S. P. Parkin, M. Hayashi, and L. Thomas, Science 320 (2008) 190.

[3] W. J. Takei, R. R. Heikes, G. Shirane, Phys. Rev. 125 (1962) 1893.

[4] F. Li, J. Yang, D. Xue, R. Zhou, Appl. Phys. Lett. 66 (1995) 2343.

[5] I. Pop, R. Muntean, O. Pop, Mater. Lett. 28 (1996) 155.

[6] S. Kokado, N. Fujima, K. Harigaya, H. Shimizu, A. Sakuma, Phys. Rev. B 73 (2006) 172410.

[7] M. S. Patwari, R. H. Victora, Phys. Rev. B 64 (2006) 214417.

[8] K. Ito, G. H. Lee, H. Akinaga, T. Suemasu J. Cryst. Growth 322 (2011) 63.

[9] Y. Takahashi, Y. Imai, T. Kumagai, J. Magn. Magn. Mater. 323 (2011) 2941.

[10] P. Monachesi, T. Björkman, T. Gasche, O. Eriksson, Phys. Rev. B 88 (2013) 054420.

[11] K. Ito, T. Sanai, Y. Yasutomi, S. Zhu, K. Toko, Y. Takeda, Y. Saitoh, A. Kimura, T. Suemasu, J. App. Phys. 115 (2014) 17C712.

[12] H. Sakakibara, H. Ando, Y. Kuroki, S. Kawai, K. Ueda, H. Asano, J. App. Phys. 117 (2015) 17D725.

[13] K. M. Ching, W. D Chang, T. S. Chin, J. Alloys. Compd. 222 (1995) 184.

[14] K. M. Ching, W. D. Chang, T. S. Chin, J. G. Duh, H. C. Ku, J. Appl. Phys. 76 (1994) 6582.

[15] Y. Yasutomi, K. Ito, T. Sanai, K. Toko, T. Suemasu, J. Appl. Phys. 115 (2014) 17A935.

[16] X. Shen, A. Chikamatsu, K. Shigematsu, Y. Hirose, T. Fukumura, T. Hasegawa, Appl. Phys. Lett. 105 (2014) 072410.

[17] M. Meng, S. X. Wu, L. Z. Ren, W. Q. Zhou, Y. J. Wang, G. L. Wang, S. W. Li, Appl. Phys. Lett. 106 (2015) 032407.

[18] K. Kabara, M. Tsunoda, J. Appl. Phys. 117 (2015)17B512.

[19] K. Kabara, M. Tsunoda, AIP Adv. 7 (2017) 056416.

[20] K. Ito, Y. Yasutomi, K. Kabara, T. Gushi, S. Higashikozono, K. Toko, M. Tsunoda, T. Suemasu, AIP Adv. 6 (2016) 056201.

[21] C. Paduani, J. Appl. Phys. 96 (2004) 1.

[22] L. Chen, J. Appl. Phys. 100 (2006) 113717.

[23] H. Wu, H. Sun, C. Chen, Phys. Rev. B 91 (2015) 064102.

[24] J. Martínez, L. Lopardo, J. Desimoni, J. Alloy & Compd. 557 (2013) 218.

[25] A. Narahara, K. Ito, T. Suemasu, Y.K. Takahashi, A. Ranajikanth, K. Hono, Appl. Phys. Lett. 94 (2009) 202502.

[26] S. Isogami, M. Tsunoda, Y. Komasaki, A. Sakuma, M. Takahashi, Appl. Phys. Express 3 (2010) 103002.

[27] H. Okumura, H. Hamaguchi, T. Koizumi, K. Balakrishnan, Y. Ishida, M. Arita, S. Chichibu, H. Nakanishi, T. Nagatomo, S. Yoshida, J. Cryst. Growth 189–190 (1998) 390.

[28] D. Dhar, O. Brandt, and H. Ploog, Appl. Phys. Lett. 86 (2005) 112504.

[29] S. Okamoto, O. Kitakami, Y. Shimada, J. Magn. Magn. Mater. 208 (2000) 102.

Figure captions

Fig. 1. Crystalline structure of antiperovskite-type Mn_4N. Face-centered II sites can be further divided into IIA and IIB sites with magnetization denoted by arrow.

Fig. 2. Emission spectrum of nitrogen plasma set at 108 W. The intensity at 336 nm was used as a measure.

Fig. 3. Out-of-plane XRD (line spectra) and RHEED (inset images) patterns along the MgO[100] azimuth. The arrows indicate the position of superlattice diffraction lines.

Fig. 4. In-plane XRD patterns of $Fe_{4-x}Mn_xN$. The scattering vector was set along MgO [200].

Fig. 5. In-plane lattice constant *a* and out-of-plane lattice constant *c* of $Fe_{4-x}Mn_xN$.

Fig. 6. Magnetization (*M*) vs. external magnetic field (*H*) curves of $Fe_{4-x}Mn_xN$ measured at RT with H_{ext} (a) perpendicular to sample surface, $Fe_{4-x}Mn_xN$ [001], and (b) parallel to sample surface, $Fe_{4-x}Mn_xN$ [100].

Fig. 7. Saturation magnetizations of $Fe_{4-x}Mn_xN$ as a function of *x* value measured at RT.

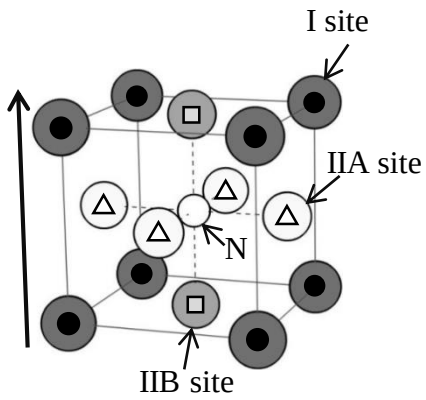

Fig. 1

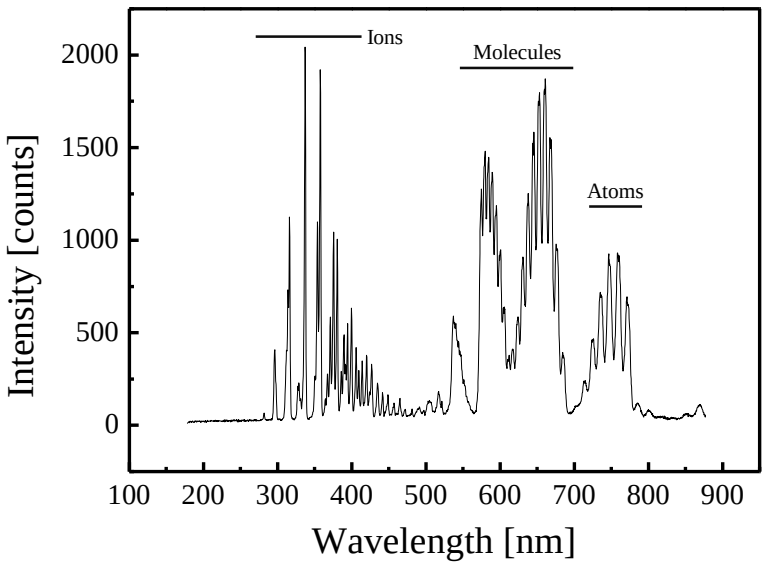
Ions
Molecules
Atoms
Intensity [counts]
2000
1500
1000
500
0
100
200
300
400
500
600
700
800
900
Wavelength [nm]

Fig. 2

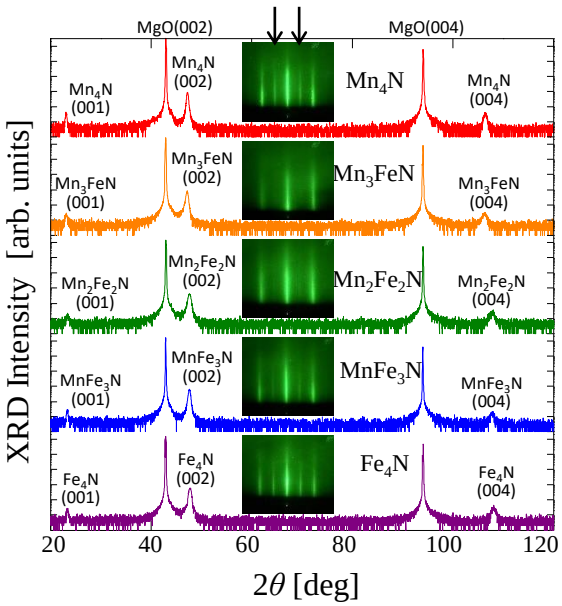
MgO(002)
MgO(004)
Mn4N (001)
Mn4N (002)
Mn4N
Mn4N (004)
Mn3FeN (001)
Mn3FeN (002)
Mn3FeN
Mn3FeN (004)
Mn2Fe2N (001)
Mn2Fe2N (002)
Mn2Fe2N
Mn2Fe2N (004)
MnFe3N (001)
MnFe3N (002)
MnFe3N
MnFe3N (004)
Fe4N (001)
Fe4N (002)
Fe4N
Fe4N (004)
XRD Intensity [arb. units]
20
40
60
80
100
120
2θ [deg]

Fig. 3

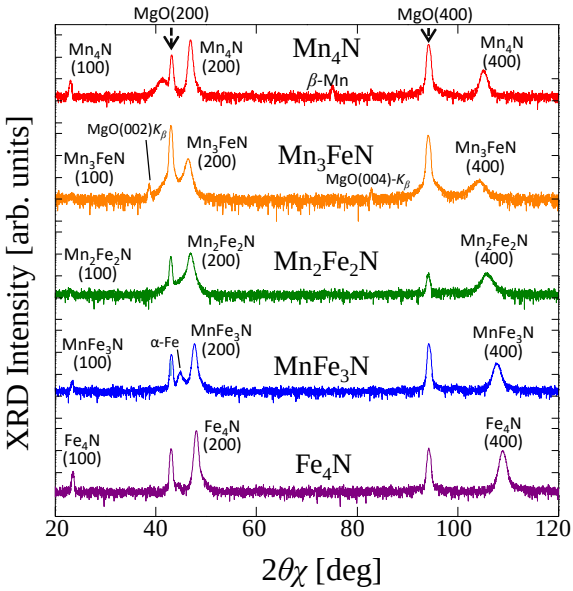
MgO(200)
MgO(400)
Mn4N (100)
Mn4N (200)
Mn4N
β-Mn
Mn4N (400)
MgO(002)Kβ
Mn3FeN (100)
Mn3FeN (200)
Mn3FeN
MgO(004)-Kβ
Mn3FeN (400)
Mn2Fe2N (100)
Mn2Fe2N (200)
Mn2Fe2N
Mn2Fe2N (400)
MnFe3N (100)
α-Fe
MnFe3N (200)
MnFe3N
MnFe3N (400)
Fe4N (100)
Fe4N (200)
Fe4N
Fe4N (400)
XRD Intensity [arb. units]
20
40
60
80
100
120
2θχ [deg]

Fig. 4

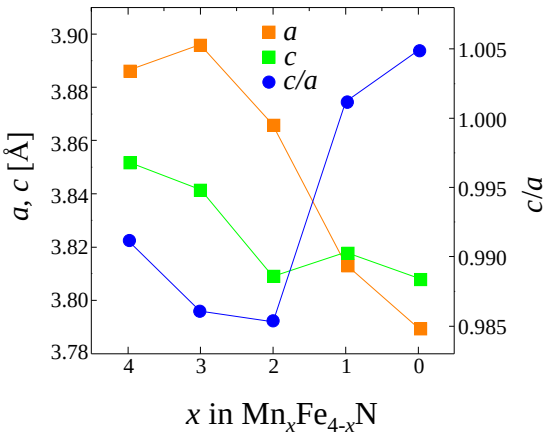
a
c
c/a
3.90
3.88
3.86
3.84
3.82
3.80
3.78
a, c [Å]
1.005
1.000
0.995
0.990
0.985
c/a
4
3
2
1
0
x in Mn$_x$Fe$_{4-x}$N

Fig. 5

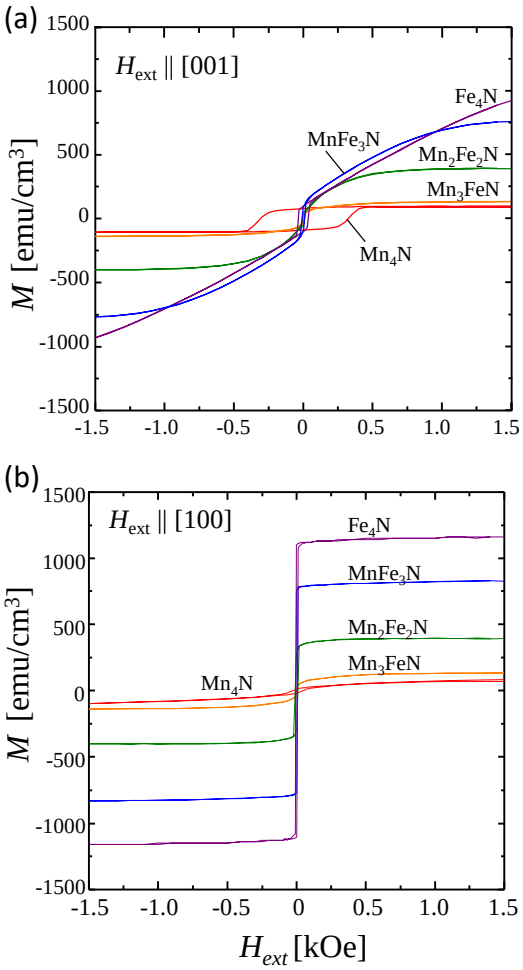
(a)
H_{ext} || [001]
Fe$_4$N
MnFe$_3$N
Mn$_2$Fe$_2$N
Mn$_3$FeN
Mn$_4$N
M [emu/cm^3]
(b)
H_{ext} || [100]
Fe$_4$N
MnFe$_3$N
Mn$_2$Fe$_2$N
Mn$_3$FeN
Mn$_4$N
M [emu/cm^3]
H_{ext} [kOe]

Fig. 6

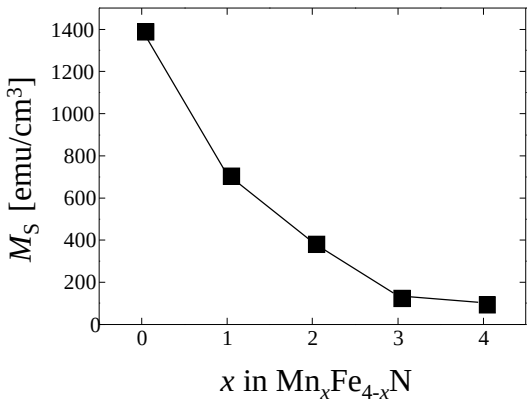

Fig. 7